Supplementary Information for

Robust growth of two-dimensional metal dichalcogenides and their alloys by active chalcogen monomer supply

Yonggang Zuo, Can Liu, Liping Ding, Ruixi Qiao, Jinpeng Tian, Chang Liu, Qinghe Wang, Guodong Xue, Yilong You, Quanlin Guo, Jinhuan Wang, Ying Fu, Kehai Liu, Xu Zhou, Hao Hong, Muhong Wu, Xiaobo Lu, Rong Yang, Guangyu Zhang, Dapeng Yu, Enge Wang, Xuedong Bai, Feng Ding, Kaihui Liu

The supplementary information includes:

Table of Contents

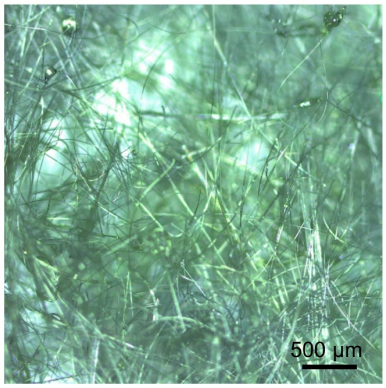

Supplementary Fig. 1 | Optical image of the silica fibre fabric after the MoS_2 growth.

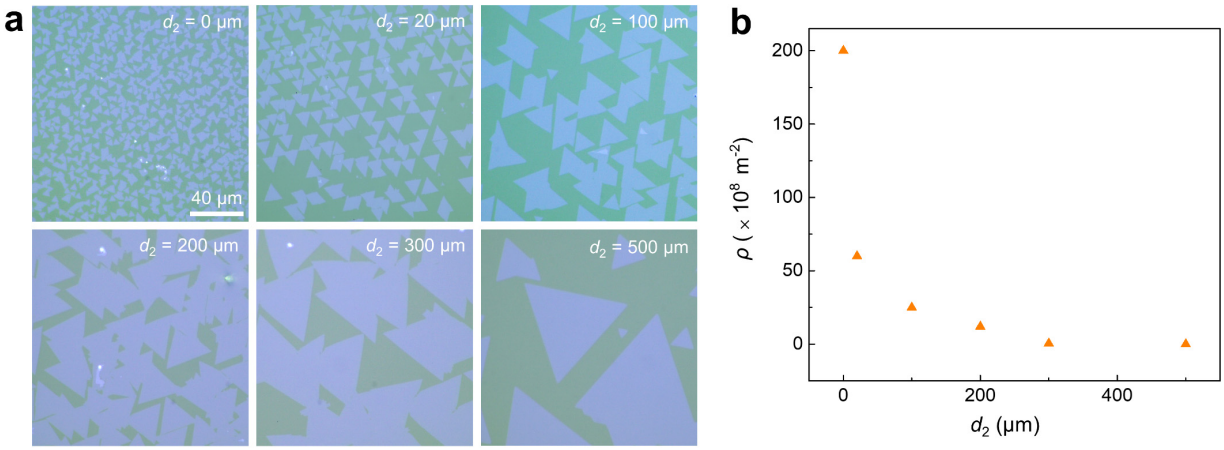

Supplementary Fig. 2 | Gap distance-dependence of the MoS_2 nucleation density on sapphire. **a**, Optical images of the as-grown MoS_2 when d_2 varied is from 0 to 500 μm. **b**, The nucleation density of the as-grown MoS_2 (orange triangle) as a function of the gap distance of d_2.

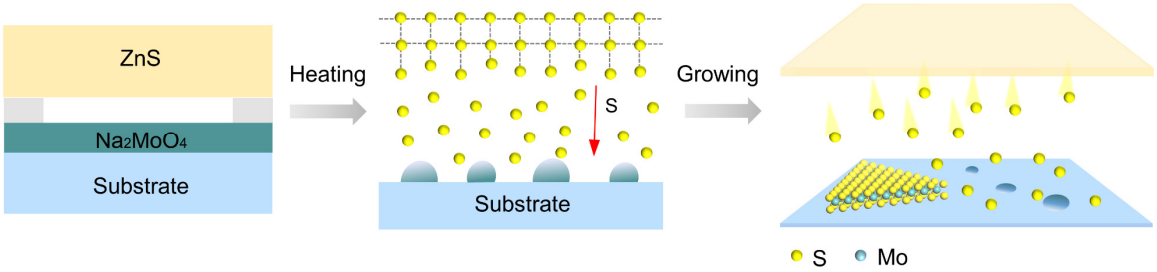

Supplementary Fig. 3 | Schematic of S monomer supply for the growth of MoS_2 when the Na_2MoO_4 was directly spin-coated on the surface of the substrate, in which d_2 is zero.

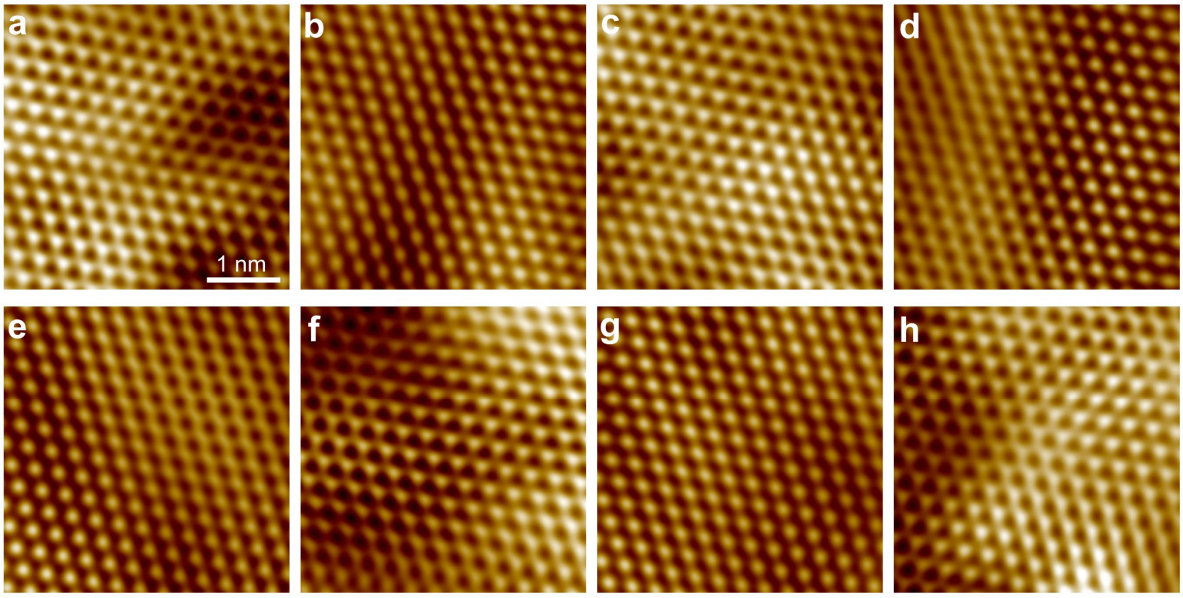

Supplementary Fig. 4 | Atomic-resolved atomic force microscopic (AFM) images of the as-grown MoS_2 samples. The S atoms are clearly resolved by AFM, which doesn't show any obvious S vacancies, confirming the ultra-low defect density in our samples.

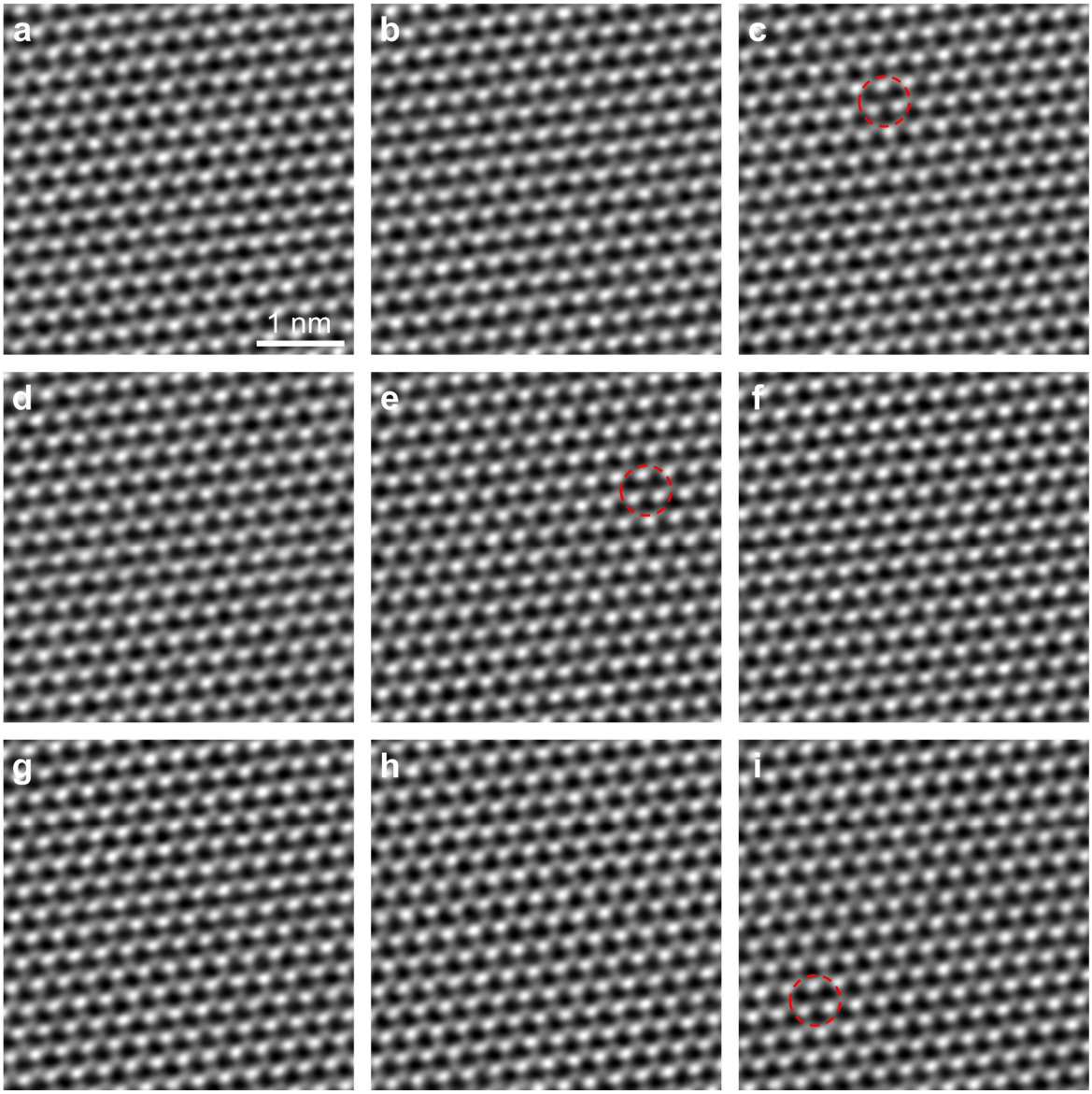

Supplementary Fig. 5 | Atomic-resolved scanning transmission electron microscopic (STEM) images captured at different regions of as-grown monolayer MoS_2. All of the images showed perfect hexagonal honeycomb lattice structure, while the low contrast sites marked by red dotted circles indicated the occasional S vacancy. The defect density was extracted at the order of ~2×10^{12} cm^{-2}.

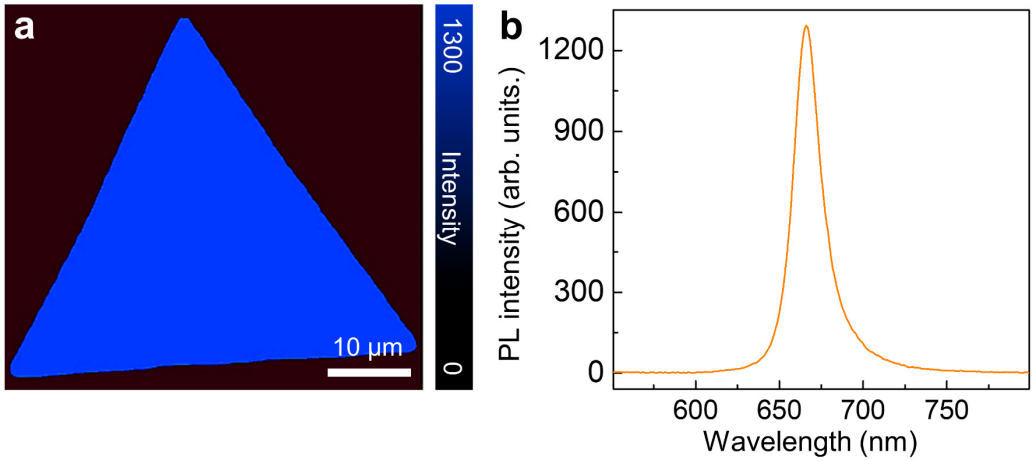

Supplementary Fig. 6 | Photoluminescence (PL) of the S-monomer-feeding-grown MoS_2. a, The PL mapping image of a whole single-crystal MoS_2 domain grown by S monomer supply. **b**, A representative PL spectrum of the as-grown MoS_2. The sharp PL peak at 667 nm (with a narrow full-width at half-maximum of 53 meV) demonstrated the high crystallinity of the sample grown by S monomer supply.

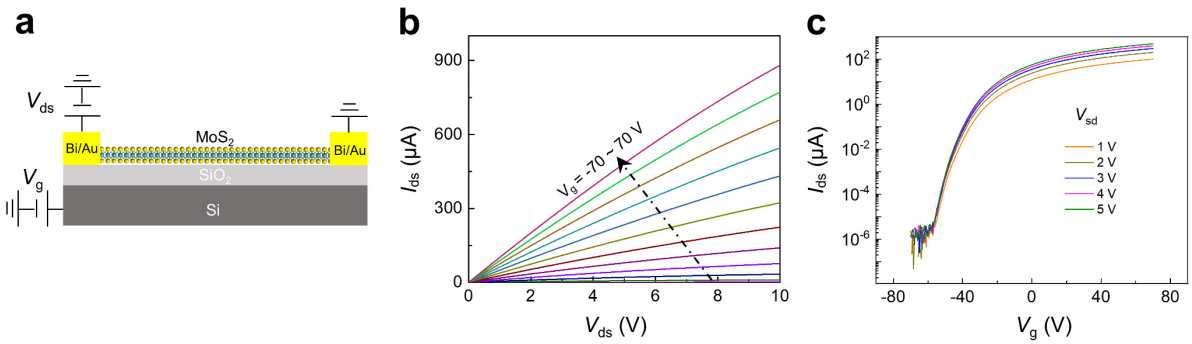

Supplementary Fig. 7 | Electronic measurements of the as-grown monolayer MoS_2 domain on SiO_2/Si substrate. a, Schematic of the monolayer MoS_2 FET device structure. **b**, Output characteristics of the FET device with gate voltage sweeping from -70 to 70 V. **c**, Transfer characteristics of the device with gate voltage sweeping from -70 to 70 V when the bias voltage is varied from 1 to 5 V. The on/off rate is ~10^8 and the threshold voltage is around -60 V.

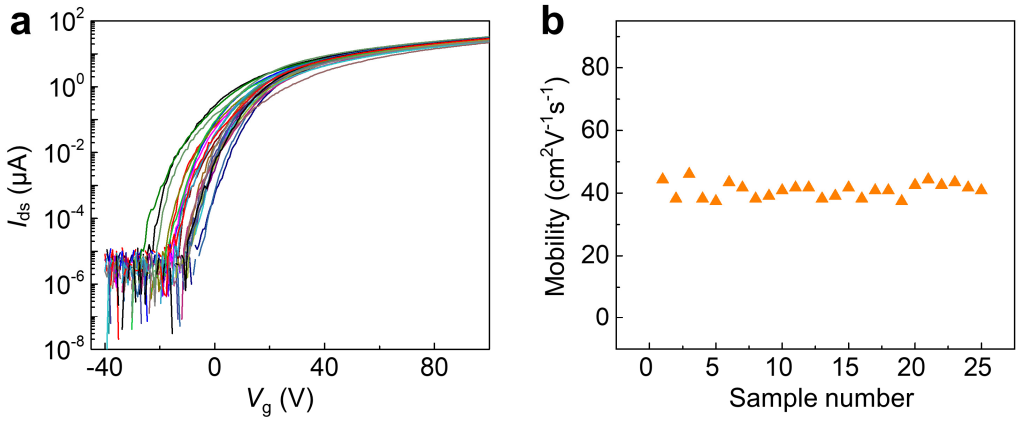

Supplementary Fig. 8 | Statistical results of the MoS_2 electrical performance at room temperature. a, Transfer curves of 25 randomly-selected MoS_2 FETs (L/W = 1) with the channel length and width of 5 μm and 5 μm respectively, at a bias voltage V_{ds} of 1V. **b**, The corresponding statistics of MoS_2 FET mobility, showing the average mobility of ~41 $cm^2V^{-1}s^{-1}$.

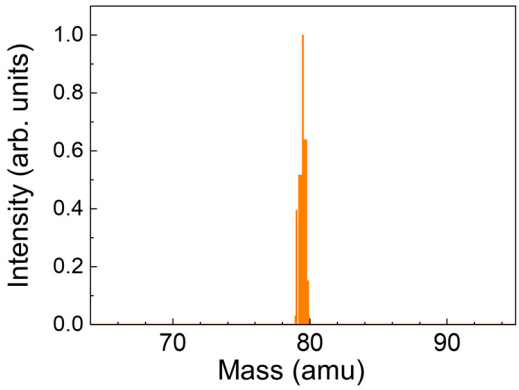

Supplementary Fig. 9 | In-situ mass spectrum of ZnSe annealed at 1000 ℃.

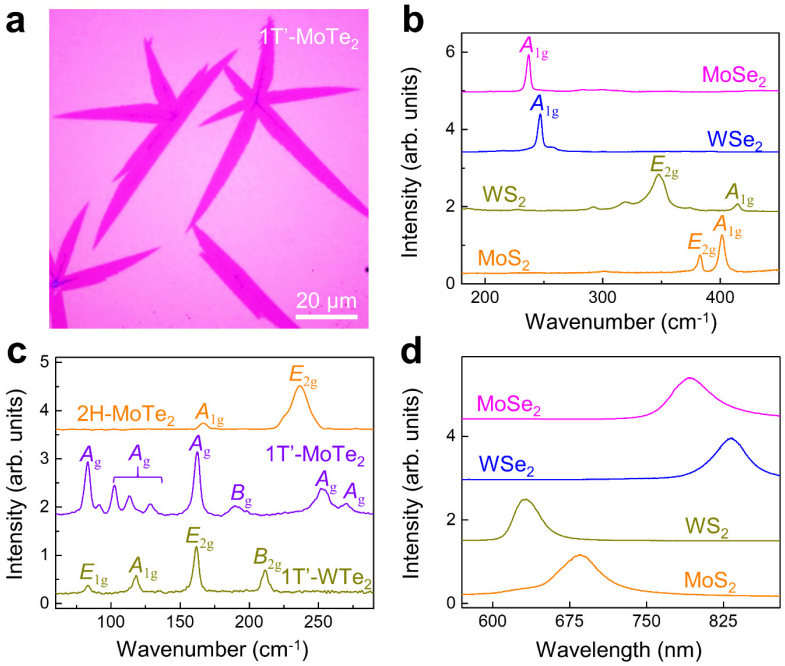

Supplementary Fig. 10 | 1T'-$MoTe_2$ sample prepared by Te monomer supply and optical measurements of diverse TMDs prepared by chalcogen monomers supply. a, Optical image of 1T'-$MoTe_2$. **b-d**, The corresponding Raman (b,c) and PL (d) spectra of as-grown TMDs. All spectra were vertically shifted for clarity.

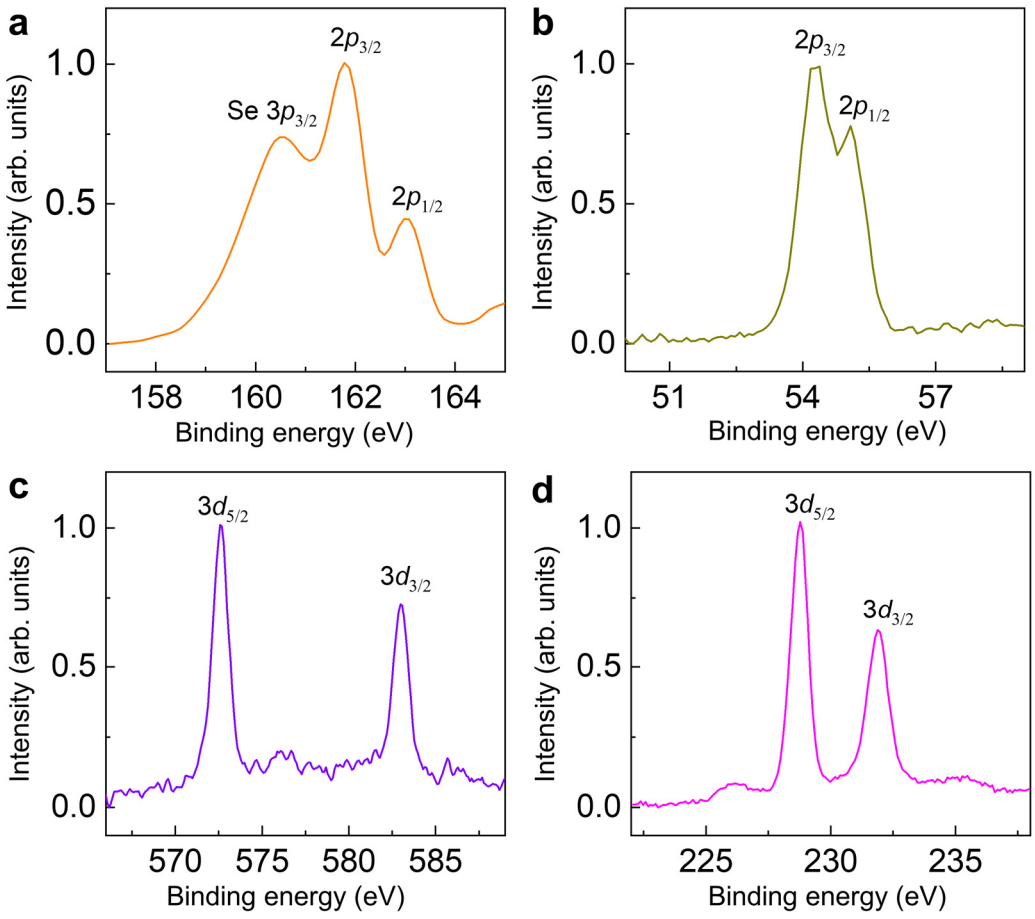

Supplementary Fig. 11 | X-ray photoelectron spectroscopy (XPS) of quaternary 2D $MoS_{2(1-x-y)}Se_{2x}Te_{2y}$ alloy. a-d, XPS spectra of as-grown $MoS_{2(1-x-y)}Se_{2x}Te_{2y}$ sample, showing binding energy states of Se 3*p* and S 2*p* (a), Se 2*p* (b), Te 3*d* (c), and Mo 3*d* (d), respectively.

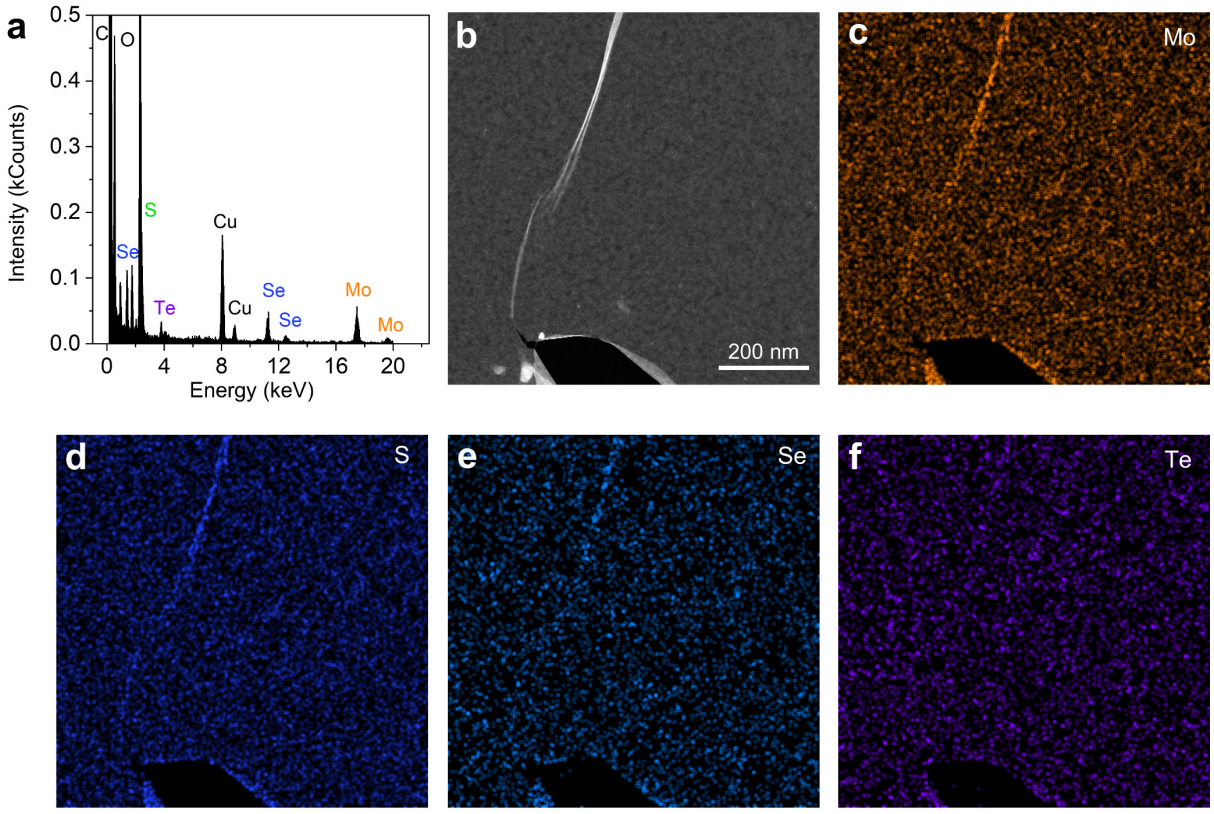

Supplementary Fig. 12 | Energy Dispersive X-ray Spectroscopy (EDS) characterization of quaternary 2D $MoS_{2(1-x-y)}Se_{2x}Te_{2y}$ alloy. a, EDS spectrum of $MoS_{2(1-x-y)}Se_{2x}Te_{2y}$ sample transferred onto TEM Cu grid. The peaks of S, Se, and Te were clearly observed, and their atomic concentrations were quantitatively extracted to be 84.0%, 12.7%, and 3.3%, respectively. **b**, The scanning transmission electron microscopy (STEM) image of the as-grown monolayer alloy film. **c-f**, EDS mapping of Mo (c), S (d), Se (e), and Te (f) corresponding to the area in (b), showing the uniform element distribution.

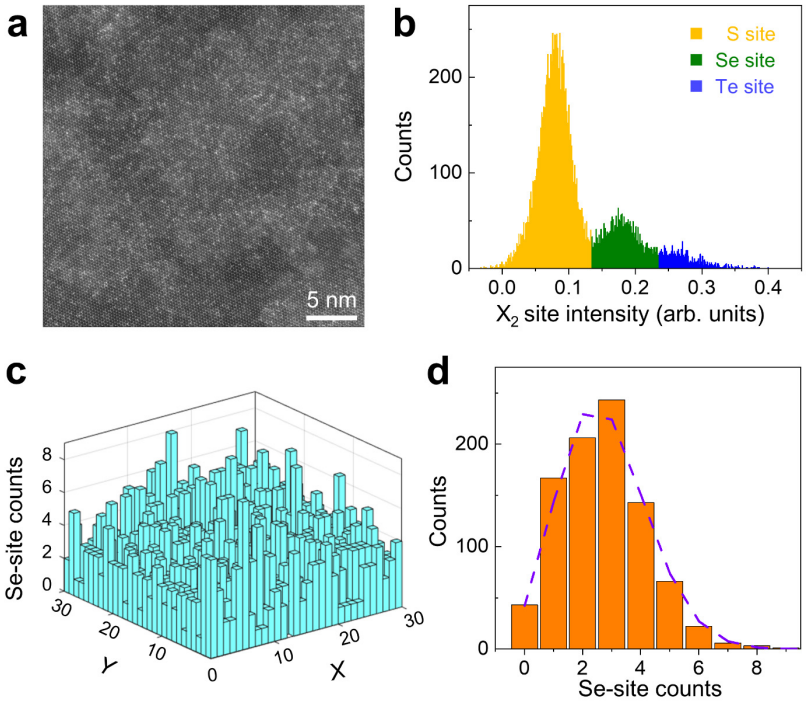

Supplementary Fig. 13 | STEM analysis of quaternary 2D $MoS_{2(1-x-y)}Se_{2x}Te_{2y}$ alloy. a, 32 × 32 nm^2 STEM image of $MoS_{2(1-x-y)}Se_{2x}Te_{2y}$ quaternary alloy. The Te-occupied sites in the image exhibit the brightest contrast and uniform distribution. **b**, Intensity histogram of the chalcogen atom (X_2) sites in (a). Due to the Z-contrast nature of STEM image, X_2 sites occupied by different atoms show distinct intensity ranges. The three peaks are assigned to be "S site", "Se site" and "Te site" regions as marked by yellow, green, and blue, respectively. The statistical result shows 9122 S sites, 2417 Se sites, and 771 Te sites from the total 12310 X_2 sites in (a). **c**, The Se-site distribution in the divided 30 × 30 parts of (a). **d**, The corresponding statistical histogram of Se-site counts in each part of (a). It shows a well binomial distribution feature (purple dotted line), revealing the random distribution of Se atoms.

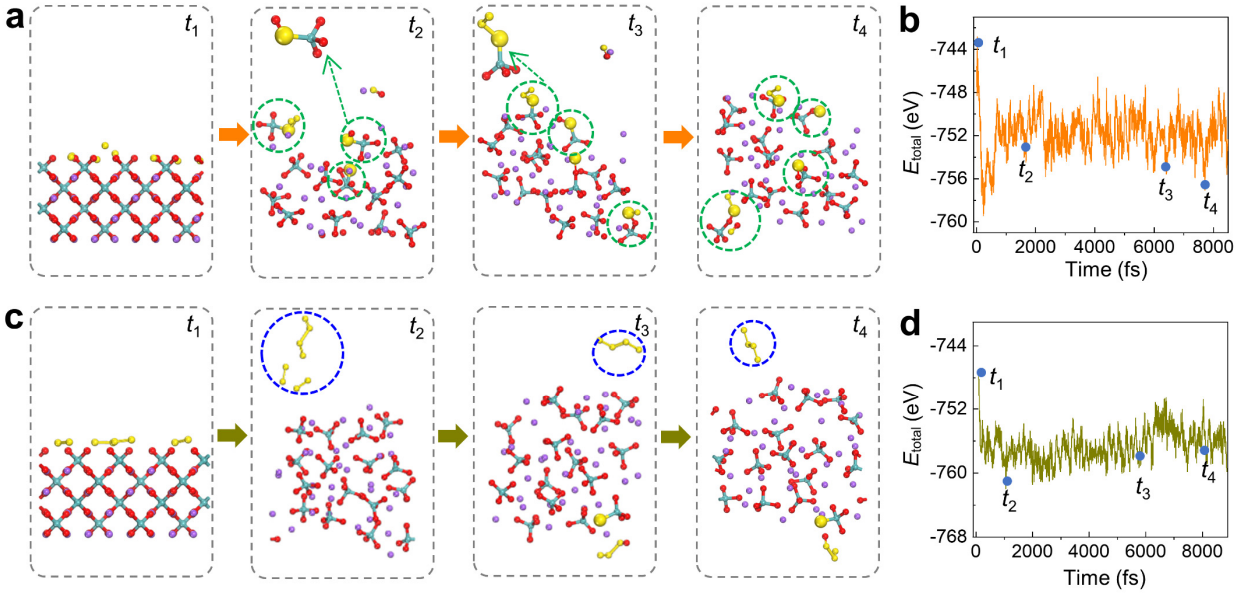

Supplementary Fig. 14 | Snapshots taken during the molecular dynamic (MD) simulation of sulfidation of liquid Na_2MoO_4 and the corresponding energy profiles. a,**b**, Snapshots taken during the MD simulation of sulfidation with eight sulphur monomers and the corresponding energy profiles at t_1 (0 ps), t_2 (1.69 ps), t_3 (6.27 ps) and t_4 (7.94 ps), respectively. It shows that S monomers can easily substitute the oxygen atoms of Na_2MoO_4. **c**,**d**, Snapshots taken during the MD simulation of sulfidation with four sulphur dimers and the corresponding energy profiles at t_1 (0 ps), t_2 (1.12 ps), t_3 (5.97 ps) and t_4 (8.00 ps), respectively. The structures in green circle presents the MoS_xO_{4-x} cluster, the ones in blue circle indicate that S dimers disappears in the form of gas. The yellow, red, violet, and blue spheres represent sulphur, oxygen, sodium and molybdenum atoms, respectively.

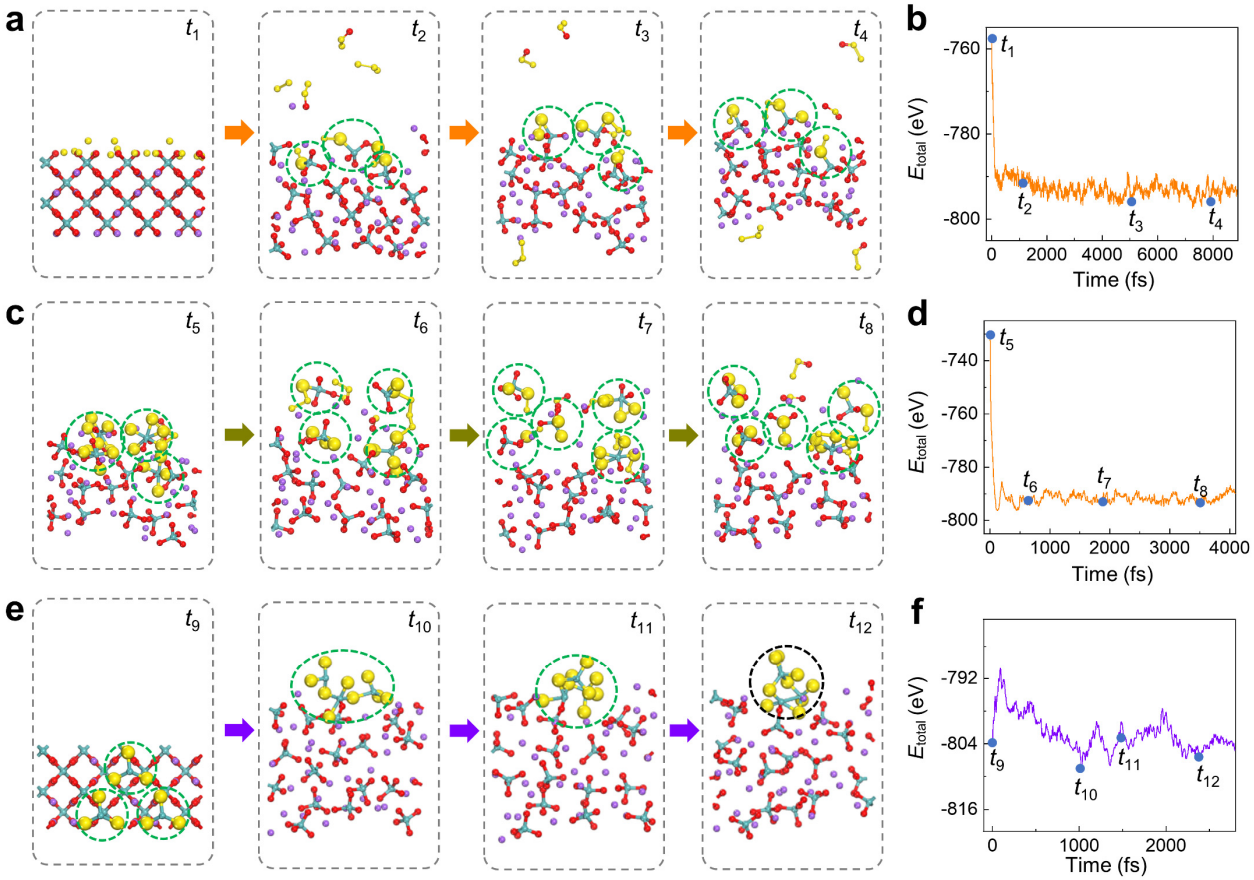

Supplementary Fig. 15 | Snapshots taken during the MD simulation on the nucleation process with S monomers supply and their corresponding energy profiles. a,**b**, Snapshots taken during the MD simulation when some sulphur monomers exist on the Na_2MoO_4 surface in the first stage and the corresponding energy profiles at t_1 (0 ps), t_2 (1.05 ps), t_3 (5.14 ps) and t_4 (8.00 ps), respectively. **c**,**d**, Snapshots taken during the MD simulation when MoS_xO_{4-x} clusters (green circle) formed on the Na_2MoO_4 surface in the second stage and the corresponding energy profiles at t_5 (0 ps), t_6 (0.62 ps), t_7 (1.92 ps) and t_8 (3.50 ps), respectively. **e**,**f**, Snapshots taken during the MD simulation when Mo_xS_y clusters (green circle) result in the nucleation of MoS_2 (black circle) in the finally stage and the corresponding energy profiles at t_9 (0 ps), t_{10} (1.00 ps), t_{11} (1.50 ps) and t_{12} (2.48 ps), respectively. The yellow, red, violet, and blue spheres represent sulphur, oxygen, sodium, and molybdenum atoms, respectively.

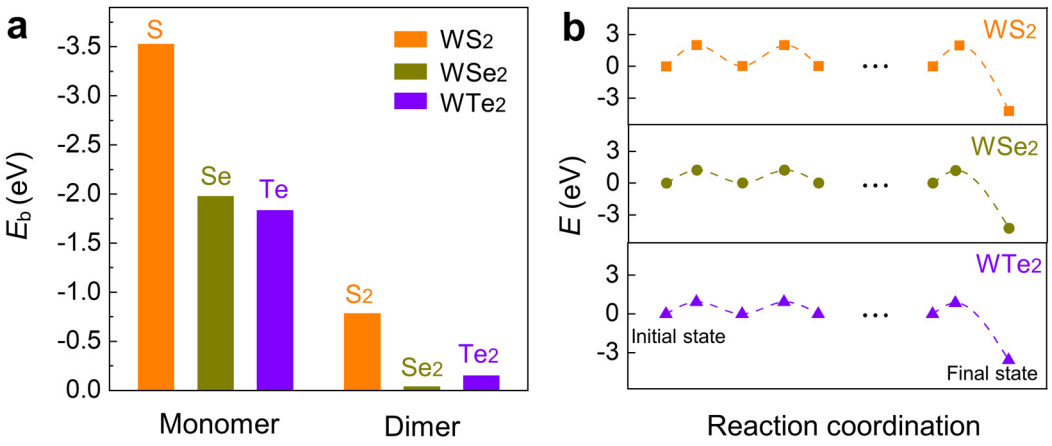

Supplementary Fig. 16 | Proposed mechanism of chalcogen monomer modulated WX_2 (X = S, Se, Te) growth. a, The binding energies of monomer and dimer on MoX_2 surface. **b**, The energy profiles of vacancy healing on WX_2 surface by using chalcogen monomers.

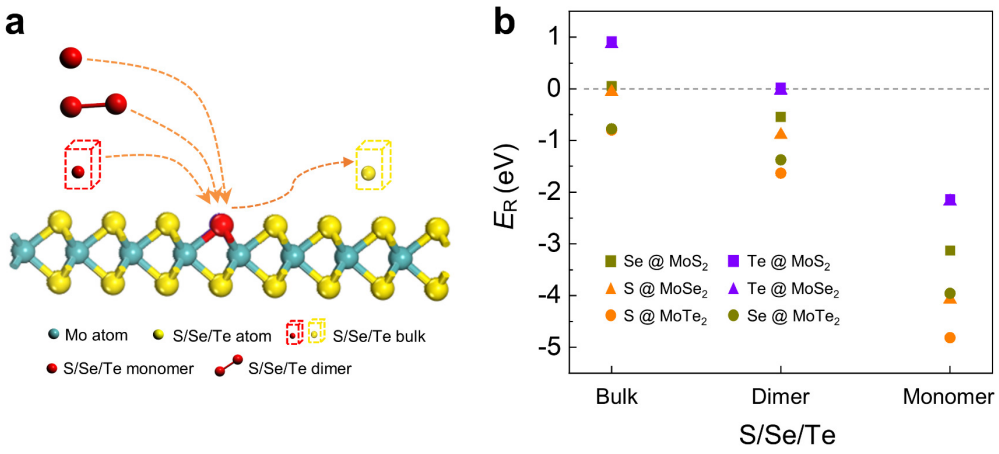

Supplementary Fig. 17 | Calculated reaction energies of trinary TMD alloys. a, The schematic diagram of substituting a chalcogen atom in a TMD by using chalcogen monomer, dimer and bulk as references. **b**, The reaction energies to form ternary TMD alloys. It can be clearly seen that the S, Se, and Te monomers can be easily doped into MoX_2 with reaction energies less than -2.0 eV, while doping of Te dimer or bulk into MoS_2/$MoSe_2$, S bulk into $MoSe_2$, Se bulk into MoS_2 are all difficult because of the near-zero or high reaction energies. These results further emphasize the advantage of S/Se/Te monomer supply to grow $MoS_{2(1-x-y)}Se_{2x}Te_{2y}$ alloy.

Supplementary Table 1. Reported S vacancy density of as-grown monolayer TMDs

Table S1	Reported S vacancy density of as-grown monolayer TMDs		
2D materials	**Fabrication method**	**S vacancy density ($\times 10^{12}$ cm^{-2})**	**Reference**
MoS_2	ME	~30	1
MoS_2	CVD	~12±4	2
WS_2	CVD	33±11 (interior) 92±45 (edge)	3
WS_2	ME	18.1	4
MoS_2	CVD	~2	This work

Note: ME, mechanical exfoliation; CVD, chemical vapour deposition.

Supplementary Note 1: Demonstrations on the supply rates of S monomer and Mo source.

In the growth system, the S monomer is released from the ZnS surface and the Mo precursor is released from the Na_2MoO_4 at high temperature. Under the experimental conditions, the relationship between the concentrations of the S monomer or the Mo precursor and the temperature follows the Boltzmann distribution law. The ratio of S monomers to ZnS and Mo precursors to Na_2MoO_4 in the system are $N_{\mathrm{S}}/N_{\mathrm{ZnS}} = e^{(-\Delta E_1/K_B T)}$ and $N_{\mathrm{Mo}}/N_{\mathrm{Na_2MoO_4}} = e^{(-\Delta E_2/K_B T)}$, respectively, where ΔE_1 and ΔE_2 are the reaction potential energies and K_B is the Boltzmann constant. N_{ZnS} and $N_{\mathrm{Na_2MoO_4}}$ can be regarded as constant values because of sufficient supply. The release rates of S monomer and Mo precursor are positively related to their concentration in the system, thus can be expressed as

$$v_{\mathrm{S}} = k_1 e^{(-\Delta E_1/K_B T)}, \quad (1)$$

$$v_{\mathrm{Mo}} = k_2 e^{(-\Delta E_2/K_B T)}. \quad (2)$$

Supplementary Note 2: Theoretical calculations on the landing probability of Mo precursor onto the substrate.

To predict the nucleation density, we only consider the collision between the Mo source and the growth substrate. There are two types of contact between the Mo source and the substrate: collision and landing. The collision is regarded as completely elastic collision, and the direction is only changed when a collision occurs. While the landing processes describe the absorption of these molecules. Supposing that every molecule either scatters away from the area between the two substrates after multiple collisions, or gets absorbed by the growth substrate, the probability (P_1) of absorption during the landing process depends on the collision frequency N, that is,

$$P_1 = \alpha \cdot \frac{1-(1-\alpha)^{2N}}{1-(1-\alpha)^2}. \quad (3)$$

Considering the velocity directions of all Mo precursors, the collision frequency (N) of the Mo precursor in direction θ at a certain distance of d can be obtained by dividing the average of the distances moved by all Mo precursors in the Z-direction before leaving the area by $2d$, that is,

$$N = \frac{L}{4dtan\theta}, \quad (4)$$

where L is the length of the substrate and α is the landing probability in one collision. For these Mo precursors in the semi solid angle, the landing probability (P) can be calculated by an integral,

$$P = \int_0^{\frac{\pi}{2}} \alpha \cdot \frac{1-(1-\alpha)^{2\cdot\frac{L}{4d\tan\theta}}}{1-(1-\alpha)^2} \sin\theta d\theta. \quad (5)$$

Therefore, the relationship between the landing probability (P) and d for Mo precursor can be described as shown in Fig. 1d.

Supplementary Note 3: Calculations of the formation energies of different transition metal dichalcogenides.

To understand the relative stability of these TMDs (MX_2, M = Mo, W; X = S, Se, Te), the formation energies of these TMDs were calculated by using

$$E_{\mathrm{f}} = E_{\mathrm{MX_2}} - \mu_{\mathrm{M}} - 2\mu_{\mathrm{X}}, \tag{6}$$

where $E_{\mathrm{MX_2}}$ is the energy of the MX_2, μ_{M} and μ_{X} are the energies of M in the form of bulk and X atoms using monomer or bulk as references, respectively. These results on formation energies (Fig. 2f) clearly show that MS_2 and MSe_2 are highly stable, while MTe_2 might hardly to be synthesized due to their high formation energies, which agrees well with the most experimental results of TMD synthesis[5, 6].

Supplementary Note 4: Statistical Se and Te atom distribution in the quaternary $MoS_{2(1-x-y)}Se_{2x}Te_{2y}$ alloy.

To evaluate the distribution of Se and Te atoms in our quaternary alloy, statistical analysis was conducted in a 32 × 32 nm^2 STEM image (Supplementary Fig. 13a). The atoms in the image were sorted into metal atom (M) sites and chalcogen atom (X_2) sites. The intensity histogram of all X_2 sites shows three peaks, which are assigned to be "S site", "Se site" and "Te site" regions, respectively, according to the Z-contrast nature of STEM image (Supplementary Fig. 13b). Note that every X_2 site in STEM image is actually a projection of two overlapped X atoms along the electron beam direction, "S site" denotes both X atoms are S, "Se site" means two possible configurations: Se-S or Se-Se, while "Te site" stands for Te-S, Te-Se, or Te-Te. According to the overall statistical result, P(S), the probability for an X_2 site to be "S site", is 9122/(9122+2417+771) = 0.741. Similarly, the probability of "Se site" and "Te site" denoting as P(Se) and P(Te), are 0.196 and 0.063, respectively.

Assume that Se and Te are randomly distributed in the X_2 sites, the overall probability of P(Se) and P(Te) will also be valid to every X_2 site. Thus, the probability of Se distribution could be calculated by the binomial distribution

$$f(k; N, P(\mathrm{Se})) = \frac{N!}{k!\,(N-k)!} P(\mathrm{Se})^k (1 - P(\mathrm{Se}))^{N-k}, \quad (7)$$

where N is the total X_2 site number of a region and k is the "Se site" number found in it. The same analysis can be applied to the Te case. To verify this random-distribution assumption, the entire image was cut into identical 30 × 30 parts, each of which comprised about 14 X_2 sites. The statistical histograms of "Te site" and "Se site" for these 900 parts are shown in Fig. 3i and Supplementary Fig. 13d, which match well with the purple dotted lines calculated by the binomial distribution, suggesting the random distribution of Te and Se atoms in our quaternary alloy.

In addition, there is a relationship between the probability P and the atom concentration c,

$$P(\mathrm{S}) = c(\mathrm{S})^2 \quad (8)$$

$$P(\mathrm{Se}) = 2c(\mathrm{Se})c(\mathrm{S}) + c(\mathrm{Se})^2 \quad (9)$$

$$c(\mathrm{S}) + c(\mathrm{Se}) + c(\mathrm{Te}) = 1. \quad (10)$$

From the probability data and these equations, the concentrations of S, Se and Te were extracted to be 86.1%, 10.7%, 3.2%, respectively, which are very close to the concentrations extracted from the preceding EDS spectrum (84.0%, 12.7%, and 3.3%, respectively, as mentioned in Supplementary Fig. 12) and confirm our statistical conclusion.

Supplementary Note 5: Theoretical calculations on initiated nucleation of MoS_2 by sulphur monomer or dimer supply.

Based on the MD simulations, the sulfidation processes of Na_2MoO_4 are analysed at atomic-level. Here we consider the sulphur source in the form of S monomers and S_2 dimers respectively. As shown in Supplementary Fig. 14, eight S monomers and four S_2 dimers were deposited on the $NaMoO_4$ surface during the MD trajectories. The MD simulations clearly showed that S monomers are more active and can easily substitute the oxygen atoms of Na_2MoO_4, resulting in SO or SO_2 molecules in the gas phase and Mo-S bond formation in the liquid $Na_2MoS_xO_{4-x}$ (green circle). This proves that S monomers released from the ZnS surface are more reactive in the growth of TMDs. Adding more S monomers to the Na_2MoO_4 surface (Supplementary Fig. 15a,b), the aggregation of Mo and S atoms during the MD simulation is clearly seen and the clusters of MoS_3O_x are formed on the surface (Supplementary Fig. 15c,d). To demonstrate the nucleation of MoS_2, we added a few MoS_3 molecules on the substrate and large Mo_xS_y clusters (green circle) were formed during the MD simulation (Supplementary Fig. 15e,f). In summary, we have demonstrated the mechanism of TMD growth by the density-functional-theory-based MD simulations. Firstly, the active S monomers replace O atoms in Na_2MoO_4. Then, the high concentration of S substitutes in the Na_2MoO_4 will lead to the formation of Mo_xS_y clusters on the surface of the substrate. Finally, the aggregation of Mo_xS_y clusters results in the nucleation of MoS_2 on the Na_2MoO_4 surface.

Supplementary Note 6: Reaction energies of ternary TMD alloys obtained by X (X = S, Se, Te) doped MoX_2.

In order to confirm the possibility of forming $MoS_{2(1-x-y)}Se_{2x}Te_{2y}$ alloy, we calculated the reaction energy (E_R) of X (X = S, Se, Te) doped MoX_2 (X = S, Se, Te). Here, we take ternary alloy $MoSe_xS_{2-x}$ as an example. Its reaction energy can be calculated by using

$$E_{\mathrm{R}} = E_{\mathrm{MoSe}_x\mathrm{S}_{2-x}} - E_{\mathrm{MoS}_2} + x\mu_S - x\mu_{\mathrm{Se}}, \tag{11}$$

where $E_{\mathrm{MoSe}_x\mathrm{S}_{2-x}}$ and E_{MoS_2} are the energies of ternary alloy $MoSe_xS_{2-x}$ and perfect MoS_2, respectively. μ_S and μ_{Se} are the energies of S and Se atoms which are in the form of bulk, dimer and monomer, respectively. The obtained different formation energies are shown in Supplementary Fig. 17. It is found that the monomers of S, Se and Te monomers can be easily doped into MoX_2 with reaction energies less than -2.0 eV. While the Te_2 could hardly be used to dope MoS_2 or $MoSe_2$ because of the near zero reaction energy. If bulk dopants are employed, only S/Se can easily dope the $MoTe_2$. This result further confirms the advantage of using S/Se/Te monomer to grow $MoS_{2(1-x-y)}Se_{2x}Te_{2y}$ alloys.

References

1. Qiu, H. et al. Hopping transport through defect-induced localized states in molybdenum disulphide. *Nat. Commun.* **4**, 2642 (2013).
2. Hong, J. et al. Exploring atomic defects in molybdenum disulphide monolayers. *Nat. Commun.* **6**, 6293 (2015).
3. Carozo, V. et al. Optical identification of sulfur vacancies: Bound excitons at the edges of monolayer tungsten disulfide. *Sci. Adv.* **3**, e1602813 (2017).
4. Jiang, J. et al. A facile and effective method for patching sulfur vacancies of WS_2 via nitrogen plasma treatment. *Small* **15**, 1901791 (2019).
5. Empante, T. A. et al. Chemical vapor deposition growth of few layer $MoTe_2$ in the 2H, 1T', and 1T phases: Tunable properties of $MoTe_2$ Films. *ACS Nano* **11**, 900-905 (2017).
6. Li, J. et al. Centimeter-scale, large-area, few-layer 1T'-WTe_2 films by chemical vapor deposition and its long-term stability in ambient condition. *J. Phys. Chem. C* **122**, 7005-7012 (2018).